225

The inviscid transonic flow about a cylinder

By NICOLA BOTTA

Institut für Strömungsmechanik, DLR Göttingen, Bunsenstraße 10, D-37073 Göttingen

The two-dimensional inviscid transonic flow about a circular cylinder is investigated. To do this, the Euler equations are integrated numerically with a time-dependent technique. The integration is based on an high-resolution finite volume upwind method.

Time scales are introduced and the flow at very short, short and large times is studied. Attention is focused on the behaviour of the numerical solution at large times, after the breakdown of symmetry and the onset of an oscillating solution have occurred. This solution is known to be periodic at Mach number between 0.5 and 0.6.

At higher speed, however, a richer behaviour is observed. As the Mach number is increased from 0.6 to 0.98 the numerical solution undergoes two transitions. Through a first one the periodical, regular flow enters a chaotic, turbulent regime. Through the second transition the chaotic flow comes back to an almost stationary state. The flow in the chaotic and in the almost stationary regimes is investigated. A numerical conjecture for the behaviour of the solution at large times is advanced.

1. Introduction

In this paper the two-dimensional inviscid transonic flow about a circular cylinder, as shown in figure 1, is investigated numerically.

As explained in Botta (1984), this flow is still subsonic for a free stream Mach number (M_∞) of 0.38. At some critical value M_∞^{cr} about 0.4 the maximal value of the Mach number, reached at the top of the cylinder, becomes one. The flow is called transonic for values of M_∞ between M_∞^{cr} and one. This is the range of speeds which is investigated here.

The transonic flow about a circular cylinder has been the subject of many investigations, both numerical and experimental.

Numerical simulations have been made, for the inviscid case, by Salas (1983), Buning & Steger (1982), Pandolfi & Larocca (1989), di Mascio (1992) and by the many contributors to the GAMM workshop at Rocquencourt (Dervieux *et al.* 1989). Pandolfi & Larocca presented a very detailed and exhaustive analysis of the flow at $M_\infty = 0.5$ and $M_\infty = 0.6$ and paved the way to the understanding of the instabilities which characterize the flow in the transonic range (see §2). The viscous transonic flow at high Reynolds numbers has been investigated, numerically, by Shang (1982) and Ishii & Kuwahara (1982).

Experimental studies of the transonic flow past a cylinder have been made by Dyment (1979), Rodriguez (1984) and Desse & Pegneaux (1990). The high-speed visualizations of Dyment, at Reynolds numbers of about 10^5, clearly show the existence, for certain values of M_∞, of two substantially different flows. This happens
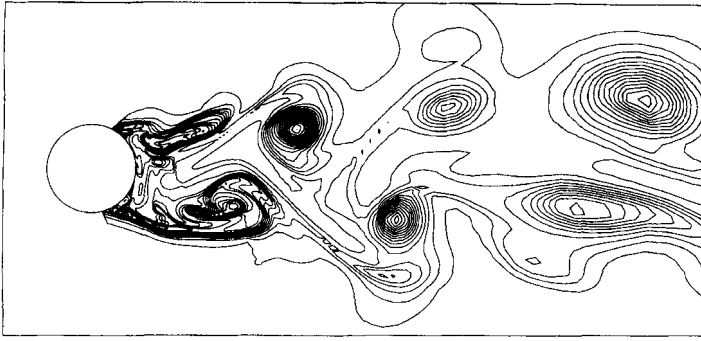
FIGURE 1. Inviscid flow about a circular cylinder at Mach 0.85: entropy contour lines.
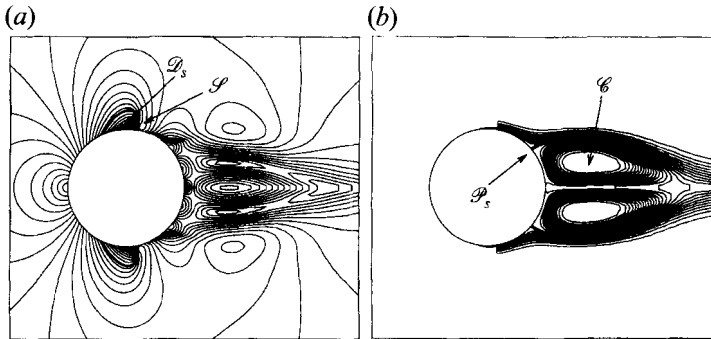
(a)   (b)

FIGURE 2. Circular cylinder at $M_\infty = 0.5$: (a) Mach number and
(b) entropy deviation contour lines; 64 × 256 cells. $t = 133$.

for $M_\infty = 0.8$ and for $M_\infty = 0.98$. In the first case both flows are unsteady. For $M_\infty = 0.98$ one flow is unsteady, the other one steady.

In the following section the transonic flow about a circular cylinder is discussed in some more detail. I will present some of the results established by Pandolfi & Larocca and focus attention on the main topics of the numerical investigation. In §3 the discretization and the initial and boundary conditions, together with some peculiarities of the implementation of the high-resolution method described in Botta (1984), are discussed. Section 4 deals with the interpretation of the numerical results. Time scales are introduced and the behaviour of the numerical solution for very short, short and large times is discussed. At the end of this section a numerical conjecture on the behaviour of the transonic flow at large times is advanced. The last section summarizes some conclusions.

2. The problem

Let me briefly recall a basic feature of the subsonic flow about the cylinder at $M_\infty = 0.38$. As explained in Botta (1994) this flow is steady and symmetric with respect to the direction of the undisturbed flow, x. Consider figure 2. In (a) a picture of the transonic flow at $M_\infty = 0.5$ is shown in terms of Mach number contour lines. In (b) the contour lines of the entropy deviation are represented. One can clearly see a supersonic region $\mathcal{D}_s$ (between the surface of the cylinder and the thick isoline $M = 1$) around the top of the cylinder. On the lee side of this region the flow returns to the subsonic regime through a radial shock wave $\mathcal{S}$. The shock causes total pressure

losses that prevent the flow wetting the cylinder from reaching the rear stagnation point on the symmetry axis. The flow separates at the point $\mathscr{P}_s$ and a circulating bubble $\mathscr{C}$ forms in the rear part of the cylinder.

Like the flow at $M_\infty = 0.38$, the flows at $M_\infty = 0.5$ and at $M_\infty = 0.6$ were among the problems proposed in the GAMM workshop at Rocquencourt. The numerical results presented for the $M_\infty = 0.38$ case in this workshop were in good agreement with each other. The ones for the $M_\infty = 0.5$ and the $M_\infty = 0.6$ cases, however, were in some way disturbing: different numerical methods designed to compute *stationary* solutions of the Euler equations produced circulating bubbles of substantially different sizes or did not converge. On the other hand, methods based on the true time integration of the full Euler equations provided very similar unsteady solutions (contributions C17, C18 and C20 in Dervieux *et al.* 1989) both for the flow at $M_\infty = 0.5$ and for the flow at $M_\infty = 0.6$.

A deeper contribution to the understanding of the behaviour of the transonic flow about the cylinder was given by Pandolfi & Larocca (1989). They used a second-order finite difference time-dependent method. The method is based on an upwind hybrid formulation of the Euler equations and consists of a blend between the λ-scheme of Moretti (Moretti 1979, 1987) and the flux difference splitting of Pandolfi (Pandolfi 1984).

For both flows ($M_\infty = 0.5$ and $M_\infty = 0.6$) they found that *the symmetric solution with a radial shock followed by inviscid separation and by the circulating bubble was unsteady*. Periodic oscillations of the shock position were coupled with a cyclic variation of the size of the bubble. For the flow at $M_\infty = 0.6$ they also observed the recurrent detachment of the circulating bubble and its advection in the wake.

Pandolfi & Larocca made their first computations on a *half*-cylinder with a flat wall aligned with the x-axis. This is equivalent to a computation over the full cylinder with the enforcement of a symmetry condition on the cells lying on the two sides of the x-axis. As they removed the wall and began to compute the flow over the full cylinder they observed, both in the $M_\infty = 0.5$ and in the $M_\infty = 0.6$ cases, that *the periodical symmetric solution is unstable*. At some critical time *the symmetry of the flow breaks down and*, after a short transient, *an asymmetric periodic flow is established*.

A short sequence of the flow at $M_\infty = 0.5$ over the full cylinder after the onset of the asymmetric periodic solution is shown in figure 3. Two radial shocks on the two sides of the cylinder oscillate alternately shedding eddies into a wake whose structure is similar to the well-known von Kármán vortex street observed in the incompressible viscous case at low Reynolds numbers.

The transition to the asymmetric periodic flow can be clearly seen in the drag and lift coefficient histories shown on figure 4(a, c). For times between zero and about 35 the flow is essentially symmetric. The lift coefficient (C_L) is about zero and the drag coefficient (C_D) tends toward a value of about 0.15. At $t \approx 35$ a first oscillation in the C_L diagram becomes visible (figure 4c). At the same time a sudden increase of the drag coefficient is observed. For $t > 50$ the asymmetric periodic flow is fully developed. The mean value of the drag coefficient is now 1.2, eight times higher than in the symmetric case! The lift coefficient exhibits wide oscillations between values of about -2.4 and 2.4. On figure 4(b, d) the spectra of drag and lift coefficients for $t \in [200, 600]$ are reported. The flow is perfectly periodic: the C_D diagram consists of two main frequencies while the lift coefficient is characterized by a single oscillation whose frequency is exactly one half of the first frequency of the drag coefficient diagram. The unsteady behaviour of the flow at $M_\infty = 0.5$ can also be described by means of the C_D, C_L diagram of figure 5. In this diagram the points $x_i = C_D(t^i)$,

$t = 326$ $t = 330.0$

$t = 327.5$ $t = 330.8$

$t = 328.3$ $t = 331.6$

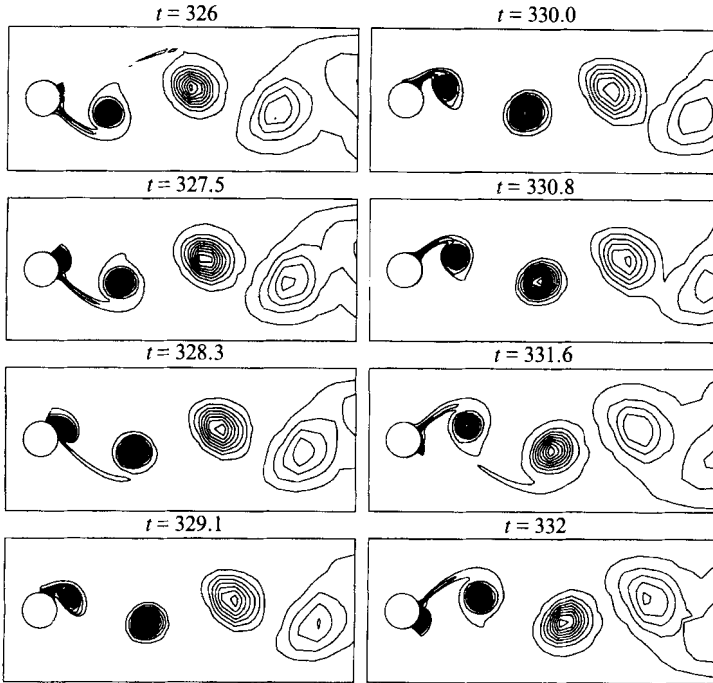$t = 329.1$ $t = 332$

FIGURE 3. Circular cylinder at $M_\infty = 0.5$: asymmetric periodic flow;
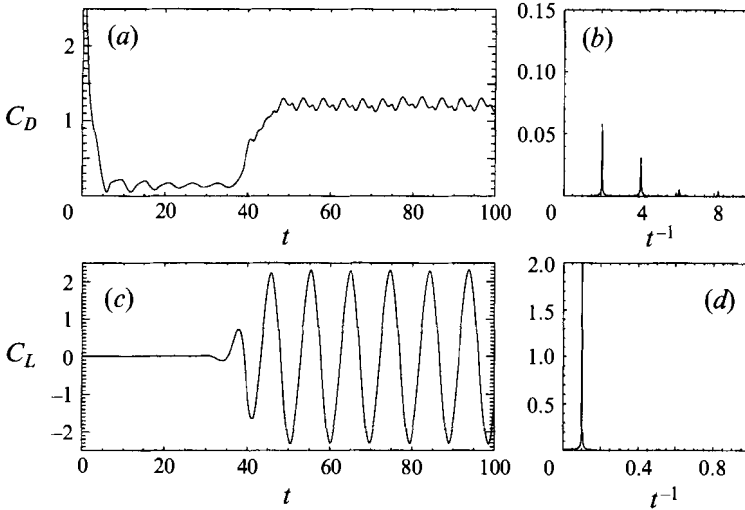entropy deviation contour lines.

FIGURE 4. Circular cylinder at $M_\infty = 0.5$: (a, b) drag
and (c, d) lift coefficients diagrams and spectra.

$y_i = C_L(t^i)$ are marked with a dot. The discrete values of the time, t^i, are chosen on the interval $[200, 600]$ to avoid the representation of the initial transient of the flow. The t^i are equally spaced with $t^{i+1} - t^i = 0.02$.

Notice that a steady solution is represented in this diagram by a single point and a periodic solution of period T by the closed orbit

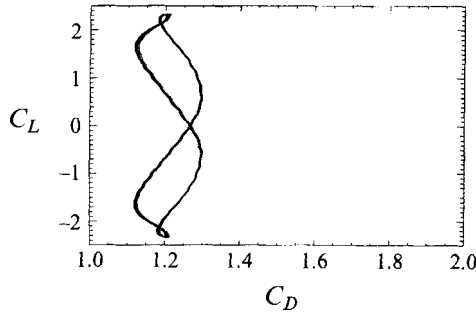$$x = C_D(t^0 + t), \quad y = C_L(t^0 + t); \quad t^0 \in I\!R, \quad t \in [0, T],$$

FIGURE 5. Circular cylinder at $M_\infty = 0.5$: C_D, C_L diagram for $t \in [200, 600]$.

$M_\infty < M_\infty^{cr}$	• steady, symmetric, stable
$M_\infty = 0.5$	∘ periodic, symmetric, unstable
	• periodic, asymmetric, stable

TABLE 1. The dependence of behaviour of the flow about a circular cylinder on the control parameter M_∞.

with $C_D(t^0) = C_D(t^0 + T)$ and $C_L(t^0) = C_L(t^0 + T)$. In the symmetric case a periodic (stationary) orbit is simply a segment (point) lying on the x-axis. The numerical results sketched above are in perfect agreement with the ones originally reported in Pandolfi & Larocca (1989). They have been confirmed by the computations of other authors, see for instance Di Mascio (1992). These numerical results show that the flow about the cylinder undergoes, as M_∞ grows above the critical value M_∞^{cr}, a bifurcation. Such a behaviour is sketched in table 1. Looking at table 1 two main questions arise:

what is the reason for the instability of the symmetric periodic flow at $M_\infty = 0.5$?
what is the behaviour of the flow for $M_\infty > 0.5$?

In §4 I will answer these questions. To do this, however, a discussion of the initial and boundary conditions and of the discretization is required. This is provided in the next section.

3. Initial and boundary condition; discretization

When Pandolfi & Larocca investigated the full cylinder, they started their computations with symmetrical initial conditions. After one integration step, however, the numerical solution was no longer *exactly* symmetric. Owing to the computer arithmetic a slight asymmetry (of the same magnitude as the round-off error of the machine) had been introduced. Remember that $a + b + c = a + c + b$ does not always hold in computer arithmetic. Thus the cell averages on symmetric cells must be updated on the basis of symmetric operands *and* of the same sequence of operations in order to conserve symmetry.

Such asymmetry has no effect on stable flows, as the results shown in Pandolfi & Larocca (1989) for the flow at $M_\infty = 0.38$ make clear. In the flow at $M_\infty = 0.5$ such asymmetry was confined, up to a critical time, to the last significant digit. Then, suddenly, the asymmetry grew and the transition to the asymmetrical periodical solution took place. This also explains why they used the 'half' cylinder with a flat wall along the x-axis to compute the symmetric unsteady solution.
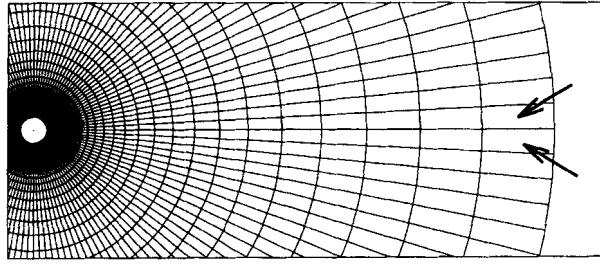
FIGURE 6. Circular cylinder: space discretization of 32×128 cells; in the perturbed initial condition only the density in the last two cells (arrows) has been altered by 10^{-6} (basic value is 1).

In my numerical computations I have followed a different, but fundamentally equivalent approach. The high-resolution finite volume method described in Botta (1994) has been implemented in such a way that, for symmetrical initial data, the numerical solution is symmetric for any time. This has been done to avoid any *numerical* source of asymmetry like that mentioned above. The code can then be used to investigate the stability of a flow in the same spirit as in a classical stability analysis: by slightly perturbing the (symmetric) initial condition.

Therefore for any given value of the M_∞ two initial conditions have been defined. The first one is symmetric and consists of the uniform flow at Mach number equal to M_∞ and pressure and density equal to one. The velocity is aligned with the x-axis:

$$\widetilde{U}_{i,j}^{0s} = (1, \gamma^{1/2} M_\infty, 0, \frac{1}{\gamma - 1} + \frac{\gamma}{2} M_\infty^2)^T, \quad i = 1, \ldots, nc1, \quad j = 1, \ldots, nc2.$$

The second initial condition is obtained from the first one by asymmetrically perturbing the values of the first component of $\widetilde{U}_{1,nc2}^{0s}$ and $\widetilde{U}_{nc1,nc2}^{0s}$ by $+10^{-6}$ and -10^{-6} respectively. These are the values of the density in the two cells shown in figure 6, by the arrows. In the numerical investigation of the flow about the cylinder at a given M_∞ a first computation is done with the symmetrical initial condition. This computation provides a symmetrical numerical solution (either steady or unsteady).

Then a second computation is done starting with the perturbed initial data. For both computations the same code, the same discretization and the same boundary conditions are used.

The characteristic based boundary conditions are those described in detail in Botta (1994).

The space discretizations consist of polar grids of 32×128 (D0), 64×256 (D1) and 128×512 (D2) cells in the radial and in the circumferential directions respectively. The 32×128 grid is the one prescribed in Dervieux *et al.* (1989) and shown in figure 6. Each grid is equally spaced in the circumferential direction and stretched in the radial direction. The stretching is such that the cells at the surface of the cylinder are almost squares, see Botta (1994). Almost all the numerical results to be discussed in the next section have been computed with the mesh D1 or D2.

In some of the computations the time step has been kept constant. In these cases the value of the CFL number was always below 0.8, depending on the M_∞ and, of course, on the time. In other computations the CFL number was set equal to 0.9 and the global time step allowed to be variable as the flow develops.
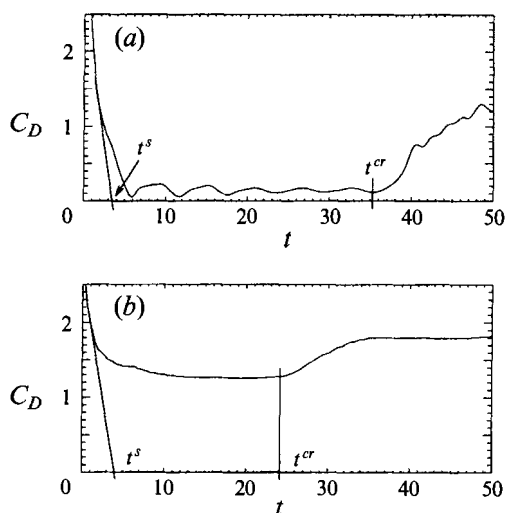
FIGURE 7. Circular cylinder at (a) $M_\infty = 0.5$ and (b) $M_\infty = 0.98$; drag coefficient diagram during the first 50 s of the numerical computation.

4. Numerical results and their interpretation

4.1. *Time scales*

Consider figure 7. In part (a) the drag coefficient history over the first 50 s† of the numerical computation has been shown for the flow at $M_\infty = 0.5$. The same diagram has been traced for the flow at $M_\infty = 0.98$ in figure 7(b). Both results have been obtained with the perturbed initial condition so that, at a critical time t^{cr}, the symmetry of the flow breaks down. In both cases, three time intervals can be naturally introduced.

A first interval, between $t = 0$ and $t = t^s$, is characterized by a fast decrease of the drag coefficient in time. This interval will be called, in the following, the interval of *very short times*. During the second time interval, for t between t^s and t^{cr}, the drag coefficient is almost constant or slowly oscillates toward some mean value. The interval $[t^s, t^{cr}]$ is designated the interval of *short times*. At $t = t^{cr}$ the breakdown of symmetry occurs. The behaviour of the flow for $t > t^{cr}$ will be referred to as the *large times* behaviour.

The drag coefficient histories to be shown in the next sections clearly indicate that the time scales of very short, short and large times can be introduced for the flows at M_∞ between 0.5 and 0.98 too. The characteristic time t^s is more or less the same and about 4. The critical time t^{cr} increases from values of about 25 for $M_\infty = 0.98$ to values of about 35 for $M_\infty = 0.5$. In the next three sub-sections the behaviour of the flow for very short, short and for large times will be presented and discussed.

4.2. *Very short times*

For very short times the behaviour of the flow about the cylinder does not depend, qualitatively, on the value of M_∞. The flow is ruled by the dynamics promoted by the initial condition. As seen in §3, apart from the small asymmetrical perturbation,

---

† Notice that the governing equations have not been written in a non-dimensional form. Thus the values of time are in seconds. Because of the unit values of density and pressure, however, such times should be divided by a factor about 280 to get the typical times for the evolution at standard conditions ($p_\infty = 101325$ Pa and $\rho_\infty = 1.29\,\mathrm{kg\,m^{-3}}$).
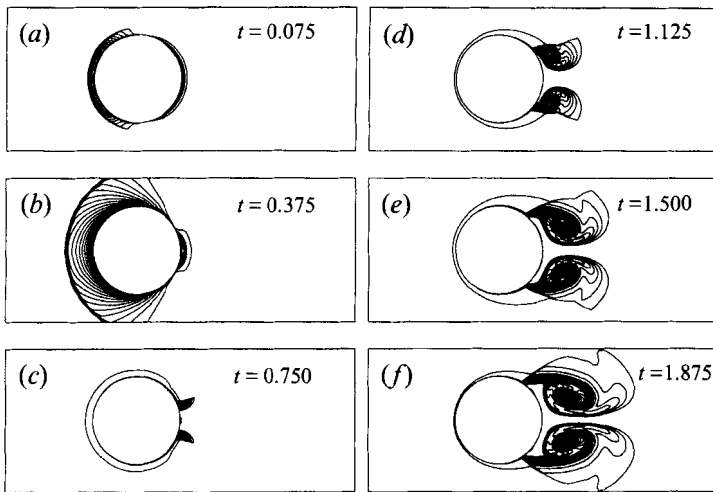
FIGURE 8. Circular cylinder at $M_\infty = 0.85$: entropy deviation contour lines: the maxima are in the cores of the vortices at the rear part of the cylinder; $t \in [0.075, 1.875]$; 128×512 cells.

this is essentially the uniform flow at Mach number equal to M_∞. Clearly such a flow does not match the boundary condition at the surface of the cylinder. Therefore at $t = 0$ a shock is generated in front of the cylinder to force the flow to comply with the boundary condition. This shock is clearly visible in figure 8(*a, b*). At the rear part of the cylinder a rarefaction wave is generated. Such a wave should not be seen in figure 8, where the entropy deviation is shown. Therefore the contour lines appearing on the rear part of the cylinder in the first two frames of figure 8 are due to the errors introduced by the discretization. Both waves travel outwards and vanish leaving a strong pressure gradient between the front and the rear of the cylinder: a cross-flow sets on. Such a flow becomes supersonic about the top of the cylinder and over expands. At the rear of the cylinder the flow re-compresses through a strong radial shock on both sides of the cylinder. The value of the Mach number in front of the shock is between 2 and 5 depending on the value of M_∞. The beginning of the formation of the radial shocks can be seen in figure 8(*c*). The flow behind the radial shocks is highly rotational and separates after a short distance from the root of the shocks. In fact the vorticity of the flow in the wake of the radial shock would be, in a stationary flow, roughly proportional to the inverse of the radial extension of the shock itself as can be argued from Crocco's theorem.

As time increases, the pressure on the rear part of the cylinder grows (remember that the drag coefficient decreases monotonically for very short times) and pushes the pair of radial shocks upstream. This can be clearly seen in figure 8(*d–f*).

Together with the radial shocks the separation point also moves upstream with a slower speed, however. This is because the shock becomes weaker as it travels upstream (where the speed of the flow is lower). Therefore the total pressure losses across the shock become less severe and the distance between the root of the shock and the separation point increases. The vorticity generated by the curved radial shocks becomes visible in the two counter-rotating vortices at the rear of the cylinder.

At $t = t^s$ the radial shocks have almost reached an equilibrium position and the decrease of the drag coefficient slows down. The flow enters a new regime which is described in the next section.
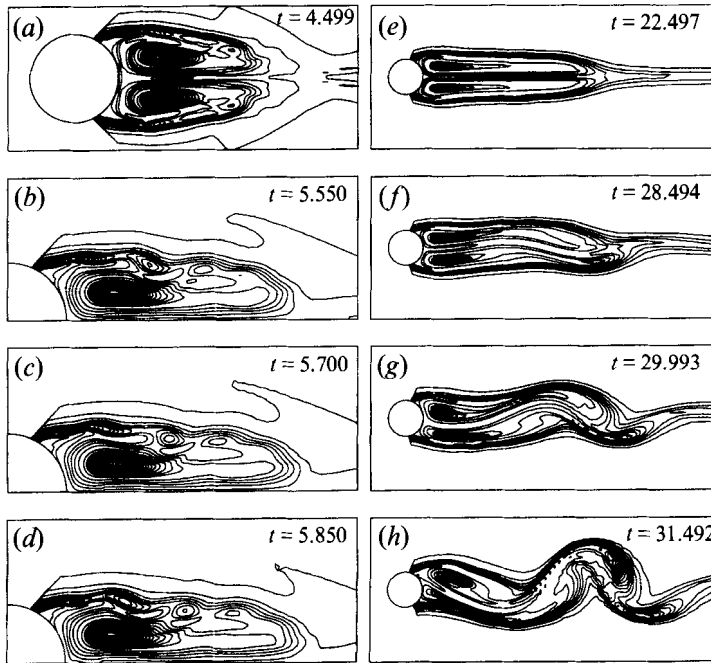
FIGURE 9. Circular cylinder at $M_\infty = 0.85$: Kelvin–Helmholtz instability at t about t^s $(a–d)$ and breakdown of symmetry at t about t^{cr} $(e–h)$; entropy deviation contour lines: the maxima are in the cores of the main vortices at the rear part of the cylinder; 128×512 cells.

4.3. *Short times*

The behaviour of the flow for short times exhibits a weak qualitative dependence on the value of M_∞. During this time interval the control parameter M_∞ begins to shape the *local* features of the flow and local instabilities occur for certain values of M_∞. The breakdown of symmetry which takes place at the critical time t^{cr}, however, is the consequence of a *global* instability of the flow which does not depend, qualitatively, on M_∞.

In the following the evolution of the flow between $t = t^s$ and $t = t^{cr}$ and the breakdown of symmetry are described for the case $M_\infty = 0.85$. Consider figure $8(f)$ again. That was the flow at $M_\infty = 0.85$ at $t = 1.875$. Between $t = 1.875$ and t about t^s the two counter-rotating vortices are stretched in the direction of the x-axis and the radial shocks and the separation points approach an almost steady position. The separation line now extends downstream over a length of about two diameters as can be seen from figure $9(a)$. Such a separation line is a contact discontinuity as well as a slip line and undergoes, for $t > t^s$, a Kelvin–Helmholtz instability. This can be seen in figure $9(a–d)$. The Kelvin–Helmholtz instability of the separation line is a local effect of small amplitude and does not have any direct influence on the breakdown of symmetry. The instability, which has been observed for other values of M_∞ as well, could be a reason for the unsteadiness, originally observed by Pandolfi & Larocca (1989), of the flow over the half-cylinder at $M_\infty = 0.5$ and at $M_\infty = 0.6$. As the time increases between t^s and t^{cr}, the vortices in the wake of the cylinder at $M_\infty = 0.85$ are stretched and become more and more elongated.

The Kelvin–Helmholtz instability of the separation line weakens and an almost steady, plane flow, in the sense that v is about zero and $u \approx u(y)$, is established in the wake of the cylinder. It is not clear whether the weakening of the instability is
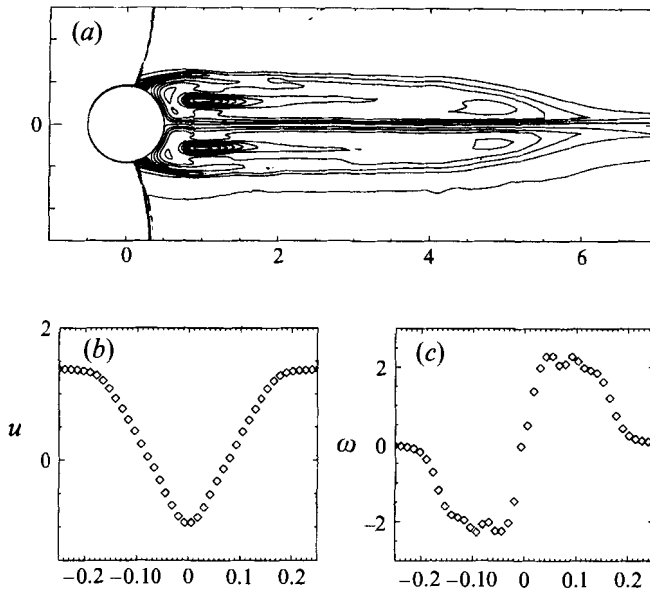
N. Botta

FIGURE 10. Circular cylinder at $M_\infty = 0.85$: (a) vorticity contour lines and (b) u-velocity and (c) vorticity distributions in the wake (x about 4); 128×512 cells.

just a numerical effect or not. Clearly as the stratified flow in the circulating bubble folds and folds and as the bubble is stretched downstream (where the discretization is rougher than in the vicinity of the cylinder), the numerical dissipation tends to smooth the flow in the wake of the cylinder. Such a flow, represented in figure 9(e) is globally unstable. The instability can be explained as follows. Consider figure 10. In part (a) the contour lines of the vorticity of the flow, ω, are shown. The distributions of u and ω along a cut of the wake at $x \approx 4$ are drawn in figures 10(b) and 10(c).

One clearly sees that $u(y)$ is a symmetric function of y (the flow is still essentially symmetric!). For $y > 0$ ($y < 0$) $u(y)$ is a monotonically increasing (decreasing) function of y with an inflection point at $y = y^*$ ($y = -y^*$), $y^* \approx 0.06$. At $y = y^*$ ($y = -y^*$) the absolute value of the vorticity has a maximum. The monotonicity of $u(y)$ and the shape of $\omega = \mathrm{d}u/\mathrm{d}y$ ensure that the conditions

$$\frac{\mathrm{d}^2 u(y)}{\mathrm{d}y^2}[u(y) - u(y^*)] \leqslant 0, \quad y = y^* \implies \frac{\mathrm{d}^2 u(y)}{\mathrm{d}y^2} = 0 \qquad (4.1)$$

are satisfied for all y in the wake of the cylinder. Such conditions are sufficient to argue the instability of an *incompressible, plane, symmetric* flow, see Drazin & Reid (1981, Chap. 22). The flow at $M_\infty = 0.85$ is clearly compressible. Notice, however, that the compressibility effects only affect the inertial terms because the basic plane flow is, by definition, divergence free: $u = u(y)$, $v = 0 \implies \nabla \cdot \boldsymbol{u} = 0$. Thus if $\mathrm{d}\rho(y)/\mathrm{d}y/\rho(y)$ is sufficiently small, the results of the linearized stability analysis of incompressible plane flows can be used to argue the instability of the compressible flow in the wake of the cylinder at $M_\infty = 0.85$. This instability, and the related breakdown of symmetry, can be observed in figure 9(f–h).

At $t \approx 28.5$ a first disturbance becomes visible in the middle of the wake. In the two layers on the upper and lower sides of the wake the self-induced motion of the vorticity (see Batchelor 1967, pp. 511–517) leads to its concentration around
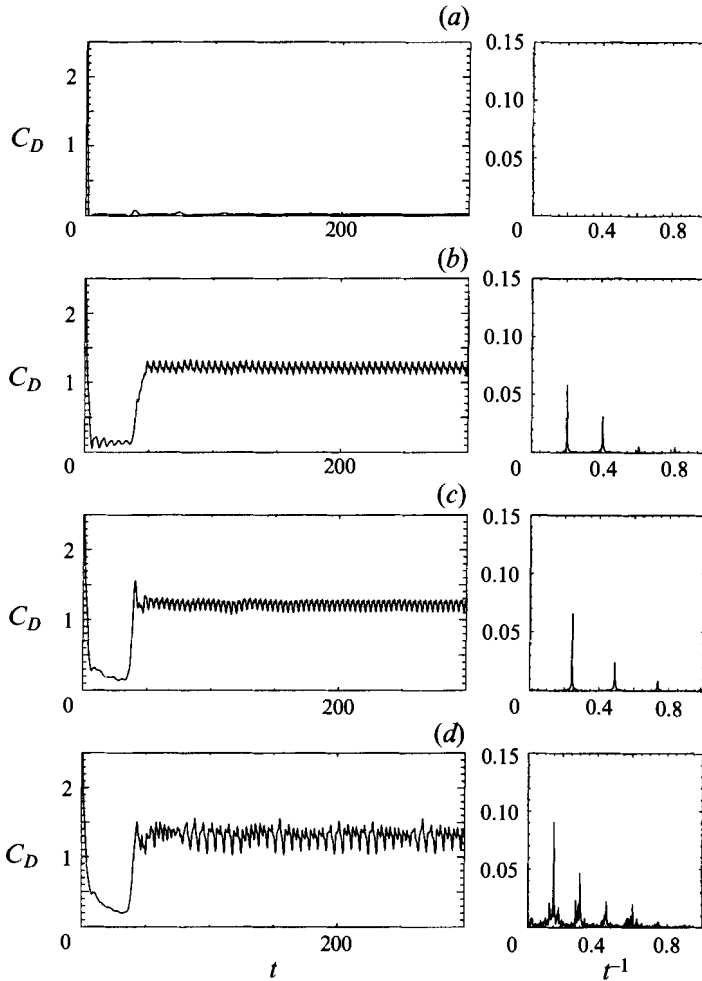
FIGURE 11. Circular cylinder at (a) $M_\infty = 0.38$, (b) $M_\infty = 0.5$, (c) $M_\infty = 0.55$ and (d) $M_\infty = 0.6$: drag coefficient diagrams for $t \in [0, 300]$ and spectra for $t \in [200, 600]$.

asymmetrical kernels (because of the different sign of ω in the two layers) and to a rapid growth of the curvature of the wake.

At $t \approx 30$ the disturbance has reached the rear part of the cylinder and begins to interact with the radial shocks. The upper shock is pushed ahead of its previous equilibrium position and weakens. The lower shock is pulled back and strengthens (figure 9h). The vortex on the upper rear part of the cylinder is about to be shed into the wake. This re-enforces the asymmetry of the wake and the process goes on. After a while an unsteady asymmetric flow is established. An instantaneous picture of this flow is shown in figure 1. The investigation of this flow at large times is the subject of the next section.

4.4. *Large times*

The behaviour of the flow about the circular cylinder at large times depends qualitatively on the value of M_∞. Consider figures 11, 12 and 13. On the left side the drag coefficient, C_D, has been plotted against the time, t, for $t \in [0, 300]$. On the
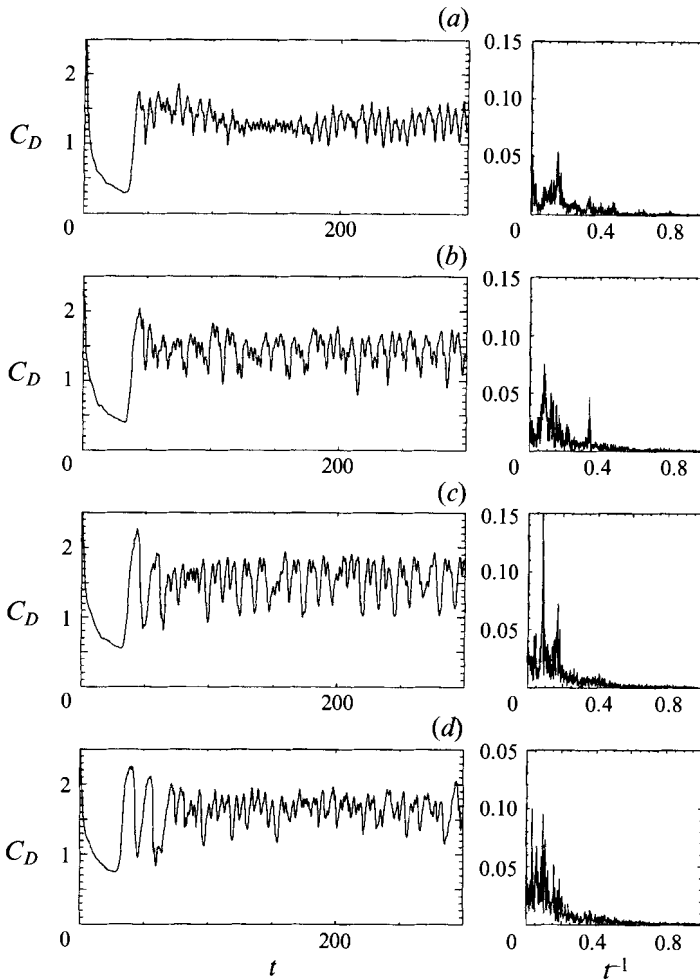
FIGURE 12. Circular cylinder at (a) $M_\infty = 0.65$, (b) $M_\infty = 0.7$, (c) $M_\infty = 0.75$ and (d) $M_\infty = 0.8$: drag coefficient diagrams for $t \in [0, 300]$ and spectra for $t \in [200, 600]$.

right the Fourier spectra of the C_D diagrams for $t \in [200, 600]$ are shown. This time interval is chosen in order to analyse the behaviour of the flow at large times. All the computations have been made with the mesh D1 (64×256 cells) and with the perturbed initial data.

Figures 11, 12 and 13 clearly show that the breakdown of symmetry is germane to the whole transonic range: in this range of velocities the symmetric solution is always unstable. Thus the introduction of time scales to study the behaviour of transonic flow is natural as claimed in §4.1.

The analysis of figures 11, 12 and 13 indicates that the flow undergoes, as M_∞ grows from 0.5 up to 1, two other transitions besides the first one, occurring at M_∞^{cr}, described in §2, see table 1. A first one, occurring at $M_\infty^{cr_1}$, leads to the breakdown of the periodic asymmetric flow and to the onset of a chaotic flow. With a second transition, at $M_\infty^{cr_2}$, the chaotic flow returns to a *quasi-steady* regime. By quasi-steady I mean here a periodic flow characterized by an oscillation of low amplitude and high frequency, see figure 13(b–d). The values of $M_\infty^{cr_1}$ and $M_\infty^{cr_2}$ seem to be about 0.6 and 0.9, respectively.
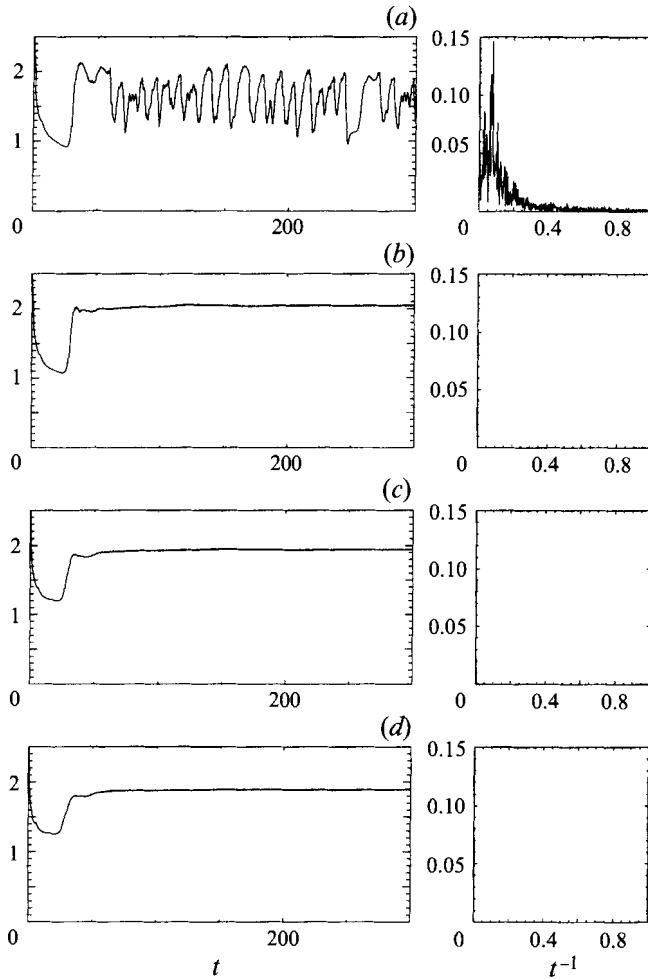
FIGURE 13. Circular cylinder at (a) $M_\infty = 0.85$, (b) $M_\infty = 0.9$, (c) $M_\infty = 0.95$ and (d) $M_\infty = 0.98$: drag coefficient diagrams for $t \in [0, 300]$ and spectra for $t \in [200, 600]$.

The comparison of the spectra at $M_\infty = 0.55$, $M_\infty = 0.6$ and $M_\infty = 0.65$ also seems to indicate that the transition to a chaotic flow is smooth, in the sense that a *quasi-periodic* flow (or actually a family of quasi-periodic flows, corresponding to some M_∞ interval) appears between the periodic and the chaotic regimes. This is the flow at $M_\infty = 0.6$. On the other hand the transition chaotic $\rightarrow$ quasi-steady, occurring at $M_\infty = M_\infty^{cr2}$, seems to be sharper.

The scenario sketched above can also be recognized in figures 14, 15 and 16 where the results of the same computations are presented in terms of lift coefficient diagrams and spectra. Of particular interest is the fact that the transition chaotic $\rightarrow$ quasi-steady is accompanied by a sudden increase of the Strouhal number, a fact well known from experiments (figure 17). The Strouhal number is a frequency (the main frequency of the C_L oscillation) times a reference time T_{ref} ($T_{ref} = L_{ref}/(a_\infty M_\infty)$, L_{ref} is the diameter of the cylinder). For the case $M_\infty = 0.98$, for instance, the computed Strouhal number is 0.44. Dyment (1979) reports, for the flow at $M_\infty = 0.98$ and $Re_\infty \approx 10^5$, a measured Strouhal number of about 0.42. Notice that, for $M_\infty < M_\infty^{cr2}$, the values of the computed Strouhal number are about 0.2 (without any significant
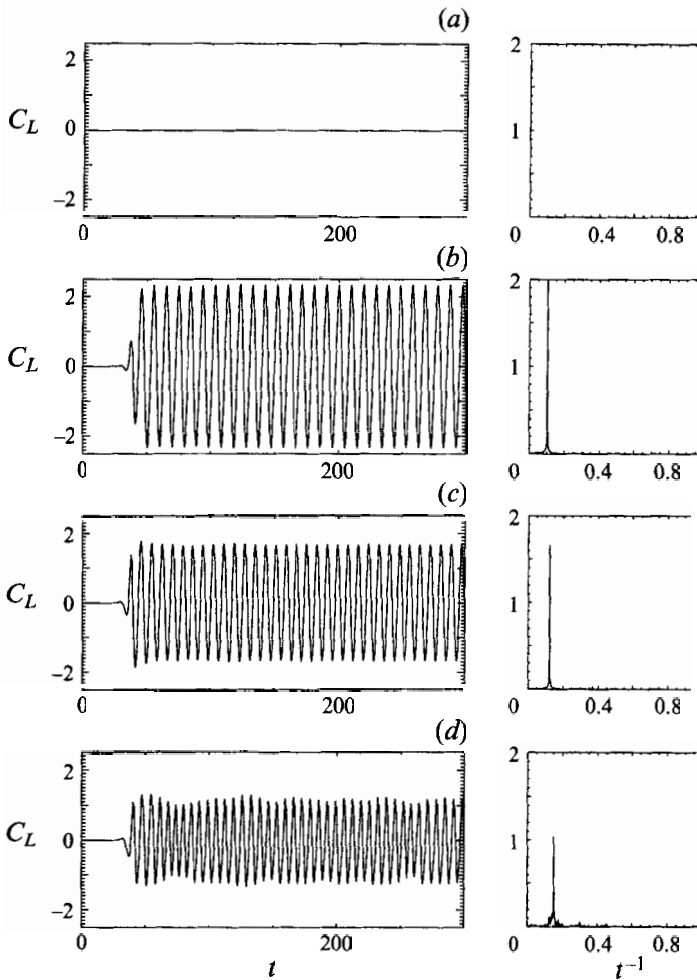
FIGURE 14. Circular cylinder at (*a*) $M_\infty = 0.38$, (*b*) $M_\infty = 0.5$, (*c*) $M_\infty = 0.55$ and (*d*) $M_\infty = 0.6$: lift coefficient diagrams for $t \in [0, 300]$ and spectra for $t \in [200, 600]$.

dependency on M_∞). This is also in very good agreement with experimental data at high Reynolds number. The experimental results reported in Dyment (1979), however, seem to indicate a value of M_∞^{cr2} between 0.95 and 0.98 (at $Re_\infty \approx 10^5$), quite different from the value 0.9 indicated by the inviscid computations. This is not surprising since there is no reason why M_∞^{cr2} (and M_∞^{cr1} as well) should not depend on the Reynolds number. In the rest of this section I will present some numerical results that indirectly confirm such a dependency by showing that the value of M_∞^{cr2} depends, in the inviscid computations, on the roughness of the grid, i.e. on the amount of numerical dissipation introduced by the discretization.

A more impressive representation of the behaviour of the flow at large times with respect to its dependence on M_∞ is given in figure 18 where C_D, C_L diagrams over the time interval $[200, 600]$ (the same interval used for the Fourier analysis) are drawn. One can clearly see how the fix-point at $M_\infty = 0.38$ suddenly turns into a closed orbit (the periodic flow at $M_\infty = 0.5, 0.55$) and then degenerates into a closed band ($M_\infty = 0.6$) and, at higher M_∞, into a more complex object ($M_\infty = 0.65$ to $M_\infty = 0.85$). Notice also the clearness of the second transition between $M_\infty = 0.85$ and $M_\infty = 0.9$.
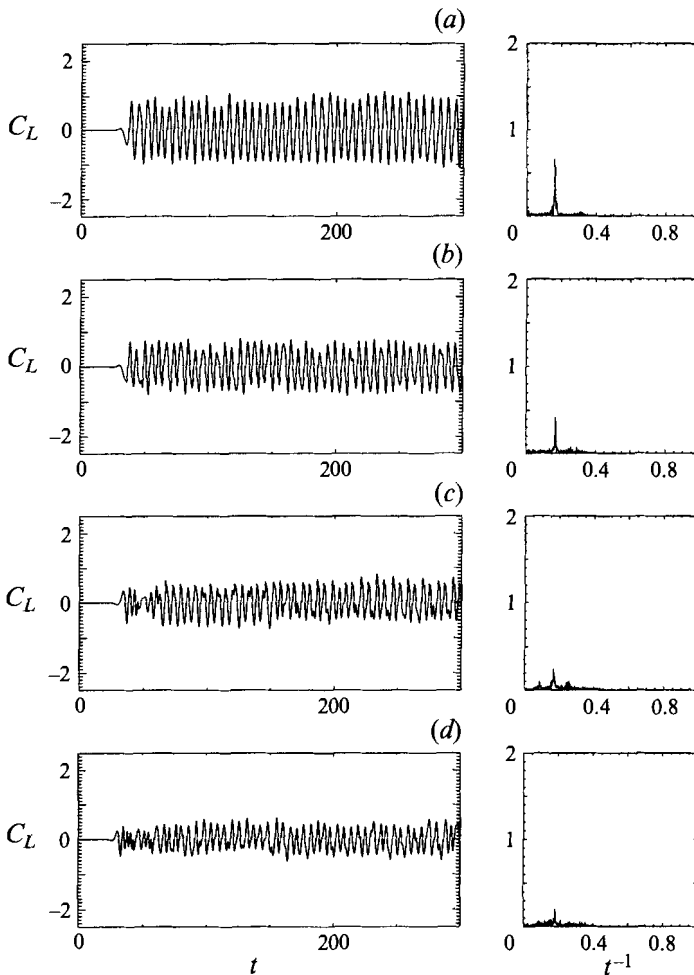
FIGURE 15. Circular cylinder at (a) $M_\infty = 0.65$, (b) $M_\infty = 0.7$, (c) $M_\infty = 0.75$ and (d) $M_\infty = 0.8$: lift coefficient diagrams for $t \in [0, 300]$ and spectra for $t \in [200, 600]$.

The numerical results described above can be summarized in table 2 which extends the observations sketched in table 1. The classification introduced with table 2 deserves some explanations. The terms *stable, unstable* and *chaotic* have been used in the following, contextual sense. For $M_\infty < M_\infty^{cr}$ *stable* means not depending qualitatively on the initial condition and on the space and time discretization. The term *unstable* appears, in table 2, only for $M_\infty > M_\infty^{cr}$. It is used to label the flow which is obtained by starting the numerical integration with the symmetric (unperturbed) initial condition. This is the flow which also has been referred to as the flow about a *half*-cylinder in §2 and §3. Thus *unstable* and *symmetric* always go together in table 2 and represent the non-relevant branch of the flow. The other branch, obtained with the perturbed initial condition described in §3, has been labelled either *stable* or *chaotic*. For $M_\infty > M_\infty^{cr}$ *stable* is used to characterize a flow which does not depend qualitatively on the discretization. For such flows no dependence on the kind of asymmetrically perturbed initial condition or on the size of the perturbation has been observed at large times. On the other hand, the term *chaotic* is used to characterize a flow which exhibits sensitivity to the choice of the discretization.
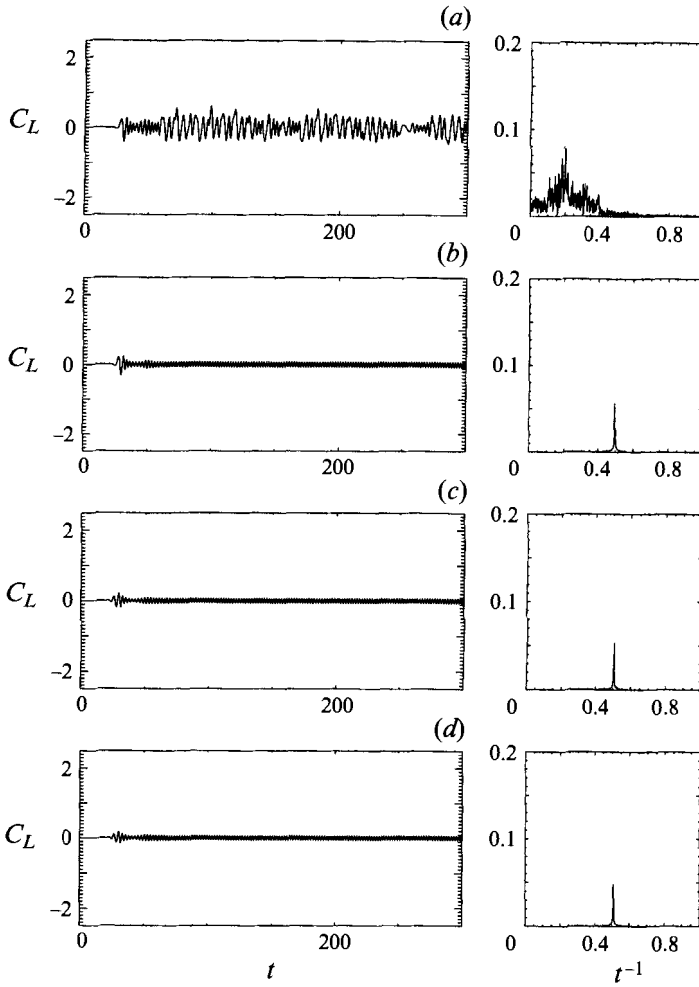
FIGURE 16. Circular cylinder at (a) $M_\infty = 0.85$, (b) $M_\infty = 0.9$, (c) $M_\infty = 0.95$ and (d) $M_\infty = 0.98$: lift coefficient diagrams for $t \in [0, 300]$ and spectra for $t \in [200, 600]$.
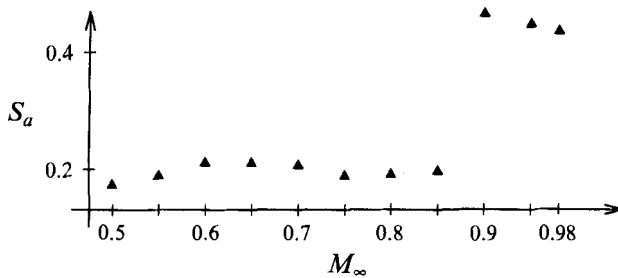

FIGURE 17. Circular cylinder: Strouhal number versus M_∞.

To make clear the above definitions and give evidence for the claims outlined in table 2, let me give a few examples of *stable* and *chaotic* flows. Consider the flow at $M_\infty = 0.5$ again. The results of two computations, made with 32×128 (a) and with 64×256 (b) cells are represented in figure 19 in terms of drag coefficient diagrams and spectra. The agreement between the two computations is very good both in the form of the C_D diagram and in the main frequencies.
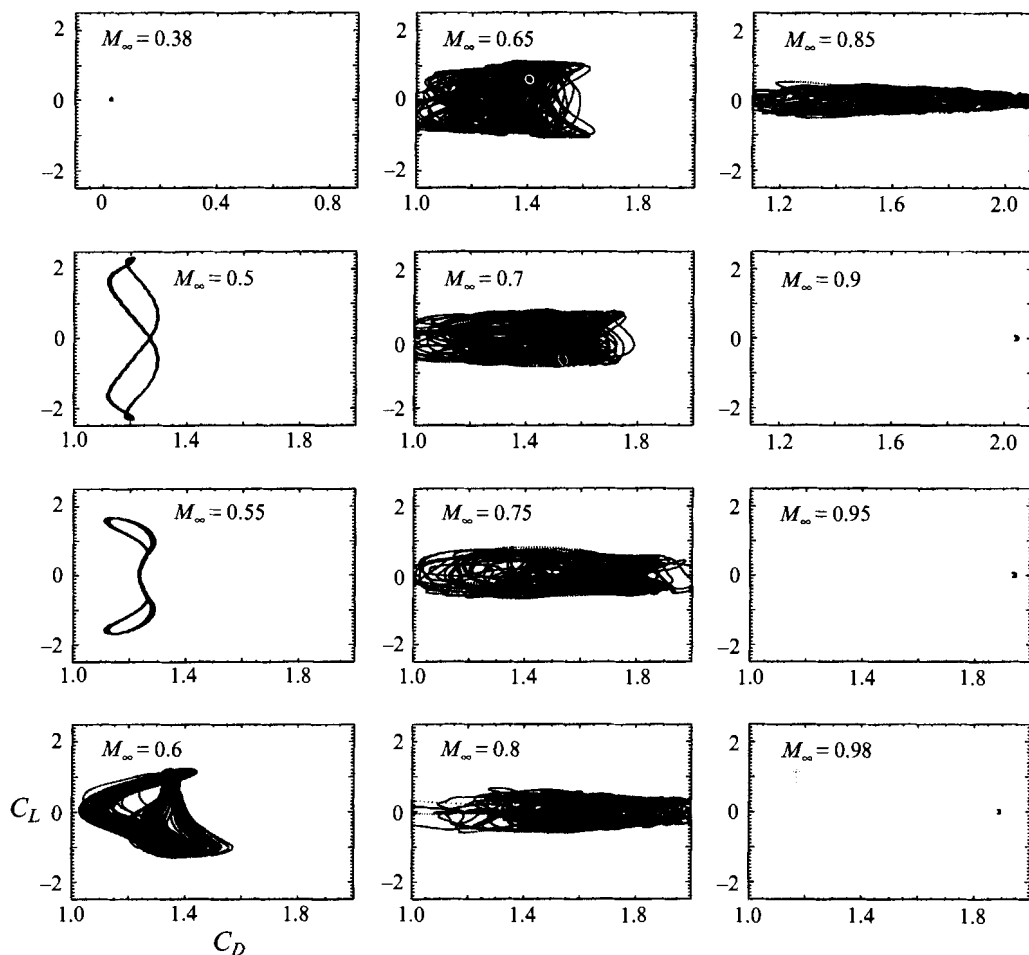
FIGURE 18. Circular cylinder at $M_\infty = 0.38$ to $M_\infty = 0.98$: C_D, C_L diagrams for $t \in [200, 600]$. Enlargement of the diagrams at $M_\infty = 0.9$, 0.95 and 0.98 reveal regular flow patterns: one such enlargement ($M_\infty = 0.9$) is shown in figure 27(f).

The same can be said of the results obtained for the flow at $M_\infty = 0.95$, reported in figure 20. Here the lift coefficient has been shown because in this case the difference between the two computations is more perceivable in this variable. The same agreement shown in figures 19 and 20 has been found, for $M_\infty^{cr} < M_\infty < M_\infty^{cr_1}$ and for $M_\infty^{cr_2} < M_\infty < 1$, between computations made on the same grid but with different time discretizations or with different initial conditions, by starting the computation with a slightly perturbed potential solution, for instance, or between computations made with different numerical techniques. To give an idea of the stability of the asymmetric periodic flow at $M_\infty = 0.5$ the reader can compare the results shown in figure 19 with those reported in figure 5 of Pandolfi & Larocca (1989). Therefore such flows are called *stable* in table 2.

Let me now turn the attention to the flows at M_∞ between $M_\infty^{cr_1}$ and $M_\infty^{cr_2}$. Such flows are claimed to be chaotic in table 2. Some characteristic features of such flows are:

(i) critical sensitivity to the discretization;

(ii) strong vortex–shock and vortex–vortex interactions;

(iii) irregular, apparently aperiodic and erratic behaviour (C_D, C_L diagrams).

$M_\infty < M_\infty^{cr}$	• steady, symmetric, stable
$M_\infty^{cr} < M_\infty < M_\infty^{cr1}$	∘ steady or periodic, symmetric, unstable • periodic, asymmetric, stable
$M_\infty^{cr1} < M_\infty < M_\infty^{cr2}$	∘ steady or periodic, symmetric, unstable • unsteady, asymmetric, chaotic
$M_\infty^{cr2} < M_\infty < 1$	∘ steady or periodic, symmetric, unstable • quasi-steady, quasi-symmetric, stable

TABLE 2. The dependence of the behaviour of the flow about a circular
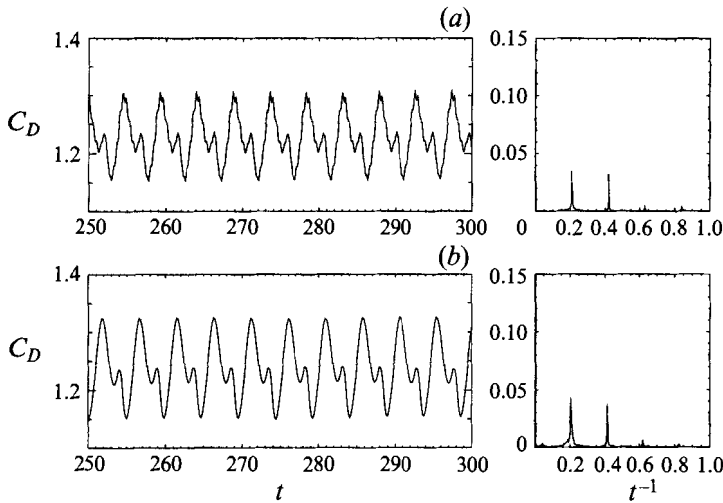cylinder dependence on the control parameter M_∞.

FIGURE 19. Circular cylinder at $M_\infty = 0.5$: computation with (a) 32×128 and with
(b) 64×256 cells; drag coefficient diagrams and spectra.

To illustrate (i) consider figure 21. For the flow at $M_\infty = 0.85$ the lift coefficient diagrams and spectra obtained with 32×128 (a), 64×256 (b) and 128×512 (c) cells are shown. The results are quite different from the ones discussed above. For each grid a quite different C_L diagram has been obtained. Notice also that, as the grid is refined, the C_L is shaped by two basic oscillations: one with bigger amplitude and lower frequency and another one with small amplitude and higher frequency (figure 21c). I will come back to this point at the end of this section.

Another example of the qualitative dependence of the solution on the mesh size is given in figure 22. In part (a) the drag coefficient diagrams and spectra of the flow at $M_\infty = 0.9$ are reported for a computation made on a discretization of 32×128 cells. In (b) the same quantities are shown for the same flow computed, this time, on a mesh consisting of 64×256 cells. The difference is striking. In the first case the flow is wildly oscillating, in the second almost stationary. This difference should not, however, be surprising. The flow at $M_\infty = 0.9$ is at the border between the chaotic range and the range of quasi-steady, stable flows (remember that I claimed M_∞^{cr2} to be about 0.9) and is precisely the qualitative difference between these two regimes that allows one to speak of a *transition* and of a *critical* value of M_∞. The point is, however, that the numerical solution may be either chaotic or quasi-steady not only in its dependence on the M_∞ but, as figure 22 clearly shows, also on the roughness of
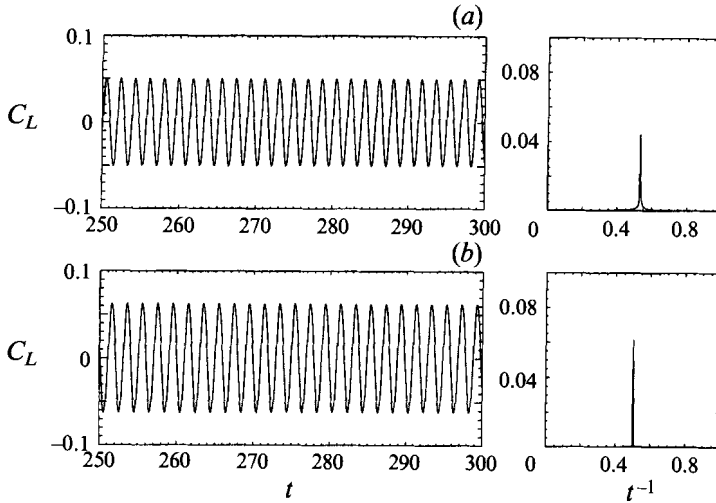
FIGURE 20. Circular cylinder at $M_\infty = 0.95$: computation with (a) 32×128 and with (b) 64×256 cells; lift coefficient diagrams and spectra.
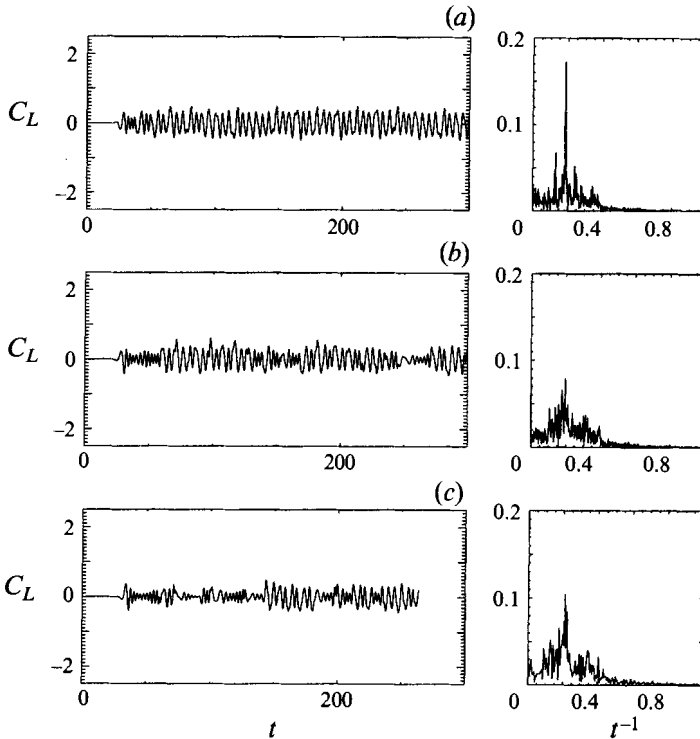

FIGURE 21. Circular cylinder at $M_\infty = 0.85$: computation with (a) 32×128, (b) 64×256 and (c) 128×512 cells; lift coefficient diagrams and spectra.

the grid, i.e. on the amount of numerical dissipation (artificial viscosity) introduced by the discretization (see also §4.4). The average of the drag coefficient over the interval [200, 600] is about 1.6 for the computation made with 32 cells and above 2 for the computation made with the finer grid. Thus the higher value of the drag coefficient, corresponding to the quasi-steady flow, is obtained with the finer grid, i.e. with a more accurate and less dissipative computation! This remark, together with that in
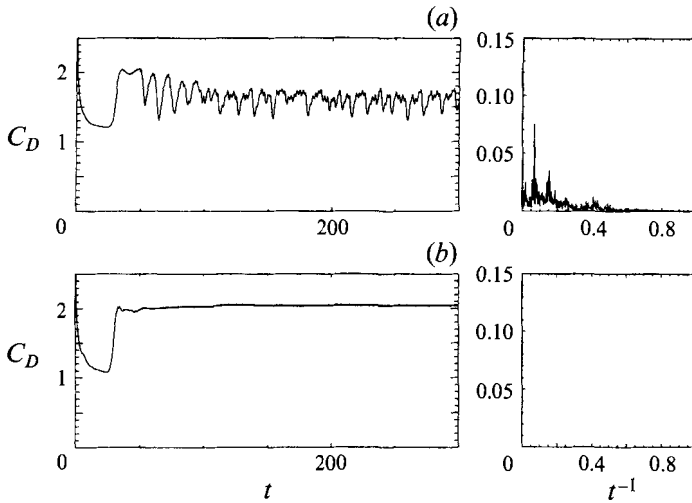
FIGURE 22. Circular cylinder at $M_\infty = 0.9$: computation with (a) 32×128 and with (b) 64×256 cells; drag coefficient diagrams and spectra.

§4.4 and in the previous paragraph suggest that the role of dissipation in presence of bifurcations might be quite subtle, see §4.5.

The differences between the flows obtained with the coarse and with the fine meshes are also evident in the lift coefficient diagrams (not shown here). In the chaotic case the amplitude of the C_L oscillation is about four times bigger than the amplitude obtained with the fine grid. This difference can also be clearly seen in figure 23 where the instantaneous contour lines of the pressure coefficient are shown for the two computations. Notice that the flow in (b) (64×256) is structurally very similar (shock position and shape, form of the wake) to the flow shown on figure 24(b), at $M_\infty = 0.95$ and again computed with a mesh of 64×256 cells. I will come back to this remark in §4.5.

Let me now turn the attention to the second topic which characterizes the flow at M_∞ between M_∞^{cr1} and M_∞^{cr2}: the interactions between vortices and shocks and between vortices themselves. Vortex–shock interaction is here understood as the process leading to the formation of *secondary shocks* which are generated in the *velocity field* induced by the *vorticity* created by the *primary radial shocks*. Such a process is well illustrated in figure 25. This is an instantaneous picture of the flow at the rear part of the cylinder at $M_\infty = 0.85$. The computation has been made on the finest grid (128×512 cells) and both the primary and the secondary shocks are well resolved. On figure 25(a) four radial shocks and one circumferential shock can be recognized. The primary ones, $\mathscr{S}_{r1}$ and $\mathscr{S}_{r2}$, are generated by the re-compression of the flow about the cylinder. Since the intensity of these shocks varies between root and tip, entropy gradients are generated downstream according to the Rankine–Hugoniot relationships. Entropy gradients are a source of vorticity which, in turn, induces a strong reversed flow. This can be clearly seen on figure 25(b). The secondary shocks $\mathscr{S}_c$, $\mathscr{S}_{r3}$ and $\mathscr{S}_{r4}$ form as the reversed flow re-compresses to comply with the boundary condition ($\mathscr{S}_c$) or with the primary flow ($\mathscr{S}_{r3}$) and ($\mathscr{S}_{r4}$).

The whole process can be described as a sort of *discrete energy cascade* in which the radial shocks play a twofold role: through each radial shock a certain amount of kinetic energy is dissipated and the rest is transferred into smaller eddies.

Another feature of the flow in the chaotic range is the appearance of aperiodic
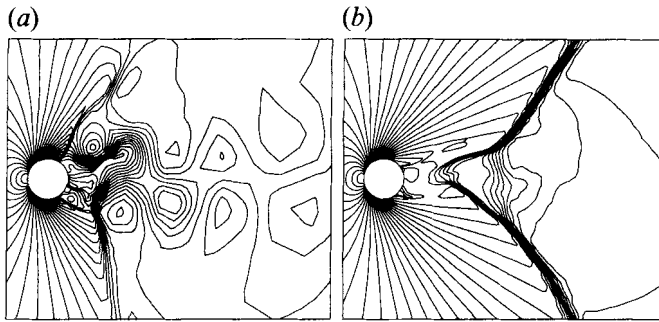
(a) (b)

FIGURE 23. Circular cylinder at $M_\infty = 0.9$: computation with (a) 32×128 and with (b) 64×256 cells; pressure coefficient contour lines.
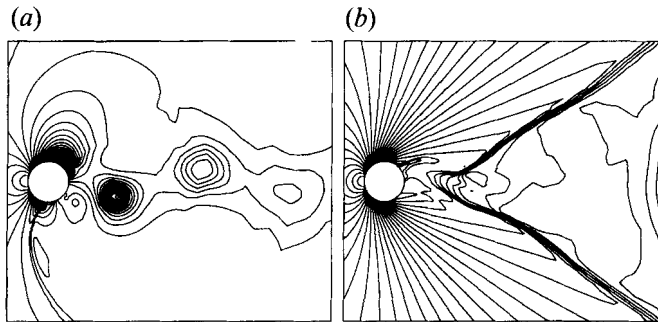
(a) (b)

FIGURE 24. Circular cylinder at (a) $M_\infty = 0.55$ and at (b) $M_\infty = 0.95$: computations with 64×256 cells; pressure coefficient contour lines.

vortex pairing in the wake of the cylinder. This is due to the fact that vortices of different size and intensity are shed at uneven time instants. Therefore the ones which are travelling downwards at a slower pace are reached by and merge with the faster ones. This can be seen in the sequence of frames of figure 26 again for the flow at $M_\infty = 0.85$.

Let me now discuss item (iii), namely the irregular, apparently aperiodic behaviour of the flow at M_∞ between M_∞^{cr1} and M_∞^{cr2}. Such irregularity can be clearly seen in figures 11 to 13 and, in particular, in the C_D, C_L representation of figure 18. To better understand the nature of the irregularity, let me focus attention on a particular flow, the one at $M_\infty = 0.85$. This flow has been the subject of a more detailed numerical investigation, consisting of computations on a 32×128, on a 64×256 and on a 128×512 grid and carried out over a long time interval. With the grids of 32×128 and of 64×256 cells the numerical integration has been carried out till t about 1000. Some of the results of these computations have already been shown, see for instance figure 21.

The results of the numerical integration made with the finest mesh of 128×512 cells have been post-processed to obtain a motion picture of the flow over the first 150 s of the time integration. The analysis of the motion picture and of the C_L and C_D diagrams over a larger interval of time clearly show that the flow wanders between two qualitatively different configurations. This possibility has already been argued in the analysis of the C_L diagrams of figure 21. One of these configuration is shown on figure 27(a). It is structurally very similar to a typical *periodic, asymmetric stable* flow at $M_\infty^{cr} < M_\infty < M_\infty^{cr1}$ like the one represented on figure 24(a). This flow
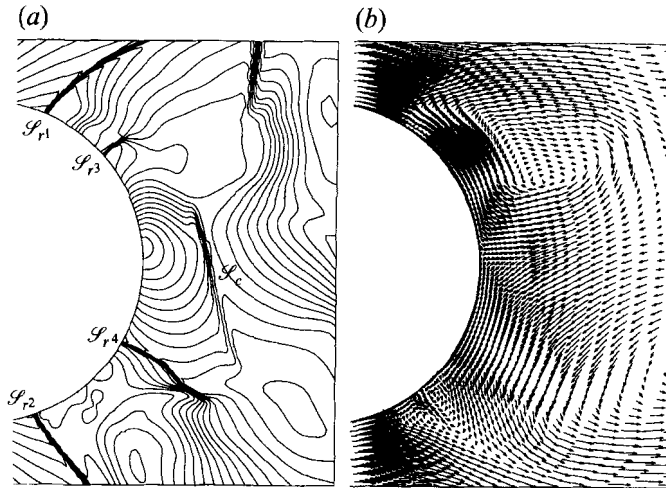
FIGURE 25. Circular cylinder at $M_\infty = 0.85$: computations with 128×512 cells;
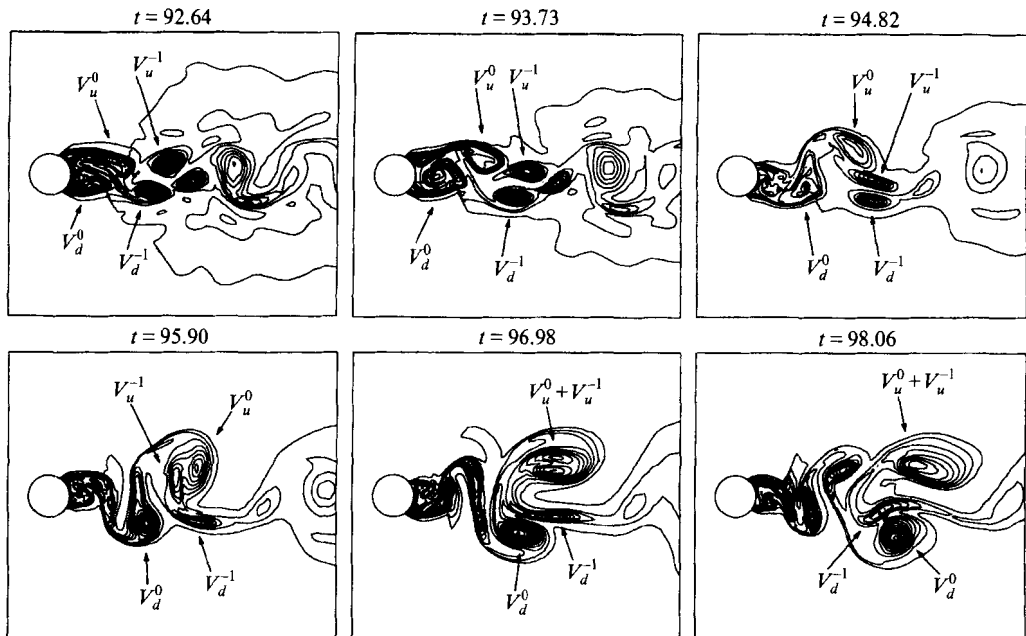(a) pressure coefficient contour lines and (b) velocity field.

FIGURE 26. Circular cylinder at $M_\infty = 0.85$: vortex pairing in the wake;
entropy deviation contour lines.

has been computed on a 64×256 grid, however. Therefore both the shock and the vortices in the wake are less resolved than in the $M_\infty = 0.85$ flow of figure 27. The other configuration, represented on figure 27(b), is similar to a typical *quasi-steady, quasi-symmetric stable* flow at $M_\infty^{cr2} < M_\infty < 1$ like the one on of figure 24(b).

Therefore the chaotic flow at $M_\infty = 0.85$ seems to have, during well defined time intervals, the features of two qualitatively different structurally stable regimes but to be unable to realize stably either one or the other. This numerical result is therefore in agreement with the experimental results obtained by A. Dyment for the flow about
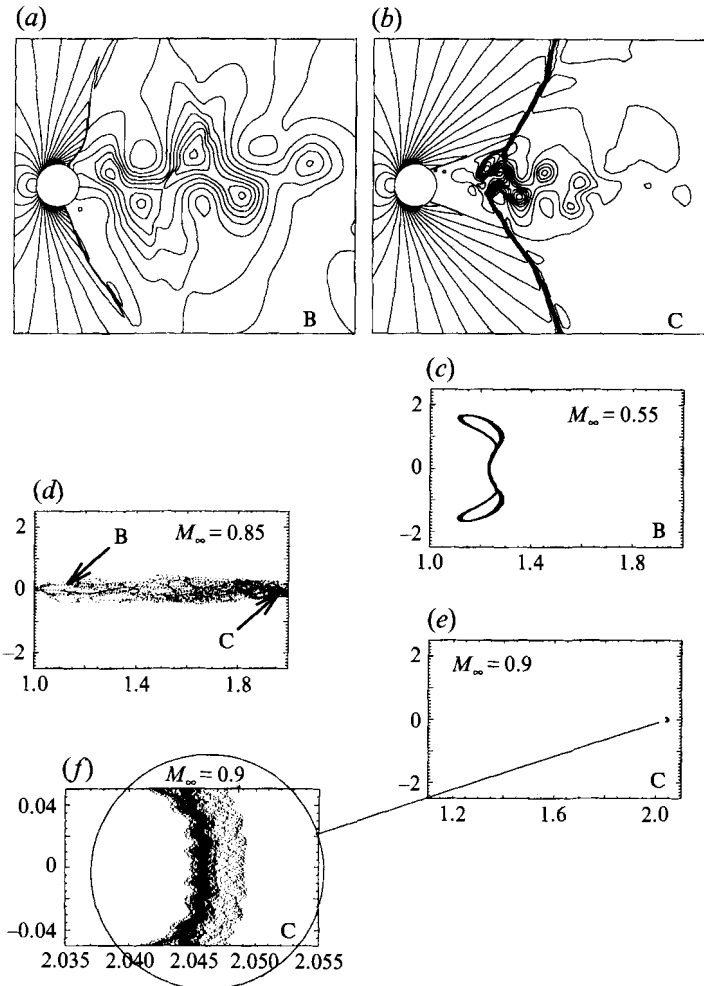
FIGURE 27. Circular cylinder at $M_\infty = 0.85$: the flow at large times wanders between two qualitatively different configurations; 128×512 cells. (a, b) Pressure coefficient contour lines; (c–f) C_D, C_L diagrams.

the circular cylinder at $M_\infty = 0.8$ and Re about 10^5 mentioned in the introduction. This can also be seen in the C_D, C_L diagrams reported in figure 27(c–f). Here the points B and C in the C_D, C_L diagram of the flow at $M_\infty = 0.85$ correspond to the states of the flow represented on figure 27(a, b): point B (low drag, wide oscillation) corresponds to (a), point C to (b). The dots represent the state of the flow at some previous or later time. The C_D, C_L diagrams should be seen as a rough attempt to introduce some representation of the *state* of the flow. Notice that this is not a trivial problem since the phase space is an infinite-dimensional space. For comparison the C_D, C_L diagrams of the flows at $M_\infty = 0.55$ and $M_\infty = 0.9$ (two instantaneous pictures of such flows can be found in figure 24) are also shown: notice the regularity of the patterns in the enlargement of the C_D, C_L diagram of the flow at $M_\infty = 0.9$ on figure 27(f).

4.5. A numerical conjecture

In the previous sections numerical solutions of inviscid transonic flows about the cylinder have been presented and discussed.
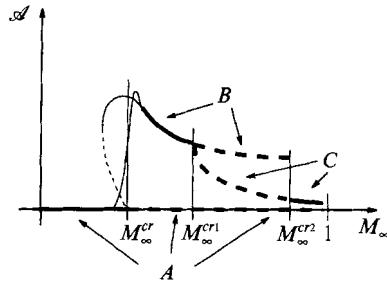
FIGURE 28. Circular cylinder: numerical conjecture upon the dependence of the flow on M_∞.

These computations are, for M_∞ between 0.38 and 0.5, in very good agreement with the results presented in Pandolfi & Larocca (1989). The same computations show, at higher M_∞, some new interesting features. Some are listed below:

(i) the appearance of transitions, periodic $\to$ chaotic and chaotic $\to$ quasi-steady, at M_∞^{cr1} and M_∞^{cr2} respectively (figure 18, table 2);

(ii) the role of dissipation in presence of the bifurcation at M_∞^{cr2} (figure 23 and §4.4);

(iii) the irregular behaviour of the numerical solution at $M_\infty = 0.85$, wandering between two different regimes (figure 27).

These peculiarities of the numerical solution can be used to formulate the following numerical conjecture upon the dependence of the Euler flow about the cylinder on the Mach number. The conjecture is illustrated in figure 28. In this picture $\mathscr{A}$ stands for some measure of the asymmetry of the flow: the amplitude of the C_L oscillation, for instance. The solid lines represent stable, the dashed lines unstable solutions. In the vicinity of M_∞^{cr} the thin lines represent two basic kinds of bifurcation which may characterize the transition from the subsonic to the transonic regime.

CONJECTURE 4.1. *For $M_\infty < M_\infty^{cr}$ a symmetric steady solution, A, exists. A is stable.*

At M_∞^{cr} a bifurcation occurs: A becomes unstable and an asymmetric periodic solution, B, appears. B is stable.

At M_∞^{cr1} a second bifurcation occurs: B becomes locally unstable and another solution, C, appears. C is locally unstable.

At M_∞^{cr2} an inverse bifurcation occurs: B disappears and C becomes stable; C is the quasi-steady, quasi-symmetric flow which is stable for $M_\infty^{cr2} < M_\infty < 1$.

Conjecture 4.1 clearly accounts for the numerical results described in the previous sections and, in particular, for the items listed above.

Thus the role of (numerical) dissipation at Mach numbers about M_∞^{cr2} is a consequence of the co-existence, in the chaotic range, of two locally unstable solutions, B and C. (A locally unstable solution is a solution which attracts the flow outside of a small neighborhood of itself.) The amount of dissipation selects whether C is stable or not. In the first case a quasi-steady, quasi-symmetric solution, like the one reported on the right of figure 23, is computed. In the second case the flow wanders between the solutions B and C just like the chaotic flow at $M_\infty = 0.85$.

5. Conclusions

The inviscid transonic flow about a circular cylinder has been investigated numerically. The computations confirm well established results for Mach numbers in the

low transonic range. At higher Mach number new phenomena have been found. In particular the transition to a chaotic, turbulent regime and, from this, back to a quasi-steady flow have been observed at $M_\infty^{cr_1}$ and at $M_\infty^{cr_2}$, respectively. The behaviour of the numerical solution both in the chaotic and in the quasi-steady regimes is in agreement with experimental results of flows at high Reynolds number.

A numerical conjecture upon the dependence of the flow on M_∞ has been advanced.

A better understanding of the transonic flow about the cylinder requires a deeper investigation of the behaviour of the flow in the vicinity of bifurcations and in the chaotic range.

As final remark I would like to stress something which is obvious: the numerical results discussed in the previous sections must not be taken as a substitute for a rigorous analytical investigation. This is because of at least two reasons. The first reason is that there is no assurance that the high-resolution method provides numerical approximations that converge, as the size of the discretization goes to zero, toward solutions of the continuous problem. The second reason is that there is no certainty that the implementation of the method is correct. These two facts explain the effort which has been undertaken, in Botta (1994), to validate the code and to critically look for possible inconsistencies between numerical results and governing equations. It is this validation work which gives confidence that the behaviour of the numerical solutions described in this paper is not just a spurious feature of the method or of its implementation.

REFERENCES

BATCHELOR, G. K. 1967 *An Introduction to Fluid Dynamics.* Cambridge University Press.

BOTTA, N. 1994 Numerical investigations of two-dimensional Euler flows: cylinder at transonic speed. Diss. ETH No. 10852, Swiss Federal Institute of Technology, Zurich.

BUNING, P. G. & STEGER, J. L. 1982 Solution of the 2-dimensional Euler equations with generalized coordinate transformation using flux vector splitting. *AIAA Paper* 82-0971.

DERVIEUX, A., VAN LEER, B., PERIAUX, J. & RIZZI, A. (Eds.) 1989 Numerical simulation of compressible Euler flows. *Notes on Numerical Fluid Mechanics. Proc. GAMM Workshop on Numerical Simulation of Compressible Euler Flows, INRIA, Rocquencourt, June 10–13, 1986.* Vieweg.

DESSE, J. M. & PEGNEAUX, J. C. 1990 Whole-field measurement of gas density from simultaneously recorded interferograms. *Exps. Fluids* **12**, 1–9.

DI MASCIO, A. 1992 Simulazione di flussi vorticosi mediante il modello di fluido compressibile non viscoso. PhD thesis, Universitá "La Sapienza", Roma.

DRAZIN, P. G. & REID W. H. 1981 *Hydrodynamic Stability.* Cambridge University Press.

DYMENT, A. 1979 Propriétés instationnaires des écoulements plans décollés. *IMF Lille* 79/60.

ISHII, K. & KUWAHARA, K. 1982 Computation of flow around a circular cylinder in a supercritical regime. *AIAA Paper* 85-1160.

MORETTI, G. 1979 The λ-scheme. *Comput. Fluids* **7**, 191–205.

MORETTI, G. 1987 A technique for integrating two-dimensional Euler equations. *Comput. Fluids* **15**, 59–75.

PANDOLFI, M. 1984 A contribution to the numerical prediction of unsteady flows. *AIAA J.* **22**, 602–610.

PANDOLFI, M. & LAROCCA, F. 1989 Transonic flow about a circular cylinder. *Comput. Fluids* **17**, 205–220.

RODRIGUEZ, O. 1984 The circular cylinder in subsonic and transonic flow. *AIAA J.* **22**, 1713–1718.

SALAS, M. D. 1983 Recent developments in transonic Euler flow over a circular cylinder. *Mathematics and Computers in Simulation* **25**.

SHANG, J. S. 1982 Oscillatory compressible flow around a cylinder. *AIAA Paper* 82-0098.